ELSEVIER

Journal of Fluids and Structures 23 (2007) 715–731

JOURNAL OF FLUIDS AND STRUCTURES

www.elsevier.com/locate/jfs

The flow between a stationary cylinder and a downstream elastic cylinder in cruciform arrangement

J. Deng, A.-L. Ren*, X.-M. Shao

Department of Mechanics, Institute of Fluid Engineering, Zhejiang University, Hangzhou 310027, People's Republic of China

Received 1 May 2005; accepted 24 November 2006
Available online 30 January 2007

Abstract

The flow past a stationary circular cylinder and a downstream elastic circular cylinder in cruciform arrangement is investigated at a constant Reynolds number of 150. The virtual boundary method is employed in this study. After the validation of the numerical method, two cases are simulated. In Case 1, both cylinders are stationary. A critical spacing is found to be about three diameters ($L/D = 3$). Beyond this critical spacing, the modification of the wake of the upstream cylinder due to the presence of the downstream cylinder is limited to the mixed region, whereas below this critical spacing, the influenced region is significantly enlarged. In Case 2, we let the downstream cylinder vibrate in response to the fluid forces acting on it, and the vibration is modeled by a spring-damper-mass system. The results show that the peak amplitude of vibrations for the cruciform arrangement is lower than that for an isolated cylinder, and the resonance region is wider than that of an isolated cylinder.
© 2007 Elsevier Ltd. All rights reserved.

Keywords: Two cylinders in cruciform arrangement; Vortex-induced vibration; Virtual boundary method

1. Introduction

Numerous experimental and numerical investigations on the flow-induced oscillation of a single cylinder have been carried out, as reviewed by Bearman (1984) and Williamson and Govardhan (2004). The interest in this class of problems emanates primarily from its practical applications in a variety of engineering flows, such as transmission lines, suspension bridges and heat exchangers. It is necessary to understand the complex phenomena exhibited by such systems. Some experimental works can be referred to: by Griffin (1971), Williamson and Roshko (1988), Ongoren and Rockwell (1988a, b) and Blevins (1990), and computational works by Mittal et al. (1991), Mittal and Tezduyar (1992), Mittal and Kumar (1999) and Zhou et al. (1999).

Hydrodynamic interactions between a cylinder and another downstream one are significant. For example, experimental results showed that the mean velocity of the wake flow is reduced due to the presence of the downstream cylinder, and the fluctuating components of the force acting on the downstream one is altered by the wake (Ohya et al., 1989; Zdravkovich, 1977). It was also observed that aerodynamic quantities such as the drag and lift forces, the pressure distribution, the Strouhal number and the vortex-shedding patterns depend strongly on the member spacing. Zdravkovich (1977) also discovered the discontinuity of those quantities at a critical spacing ratio L/D ranging between

*Corresponding author. Tel.: +86 571 87952200.
E-mail address: renanlu@zju.edu.cn (A.-L. Ren).

0889-9746/$ - see front matter © 2007 Elsevier Ltd. All rights reserved.
doi:10.1016/j.jfluidstructs.2006.11.005

3.5 and 4. For the vortex-induced vibration involving two cylinders in tandem, staggered or side-by-side arrangement, one can make reference to Zdravkovich (1985), Brika and Laneville (1999), Liu et al. (2001), and Mittal and Kumar (2001).

For Case 1, where two stationary cylinders are arranged perpendicular to each other, the complex flow structures have been investigated experimentally (Fox and Toy, 1988a, b; Fox, 1991). The experiments were performed in a wind tunnel at a Reynolds number of 2×10^4, and in a water tunnel facility at a Reynolds number of 2×10^3, respectively. The results showed that the structures of the turbulence developed in the cross geometry are of considerable importance to the design and analysis of the associated thermohydraulic mechanics. It was suggested that the turbulence at the center of the configuration may lead to increased heat transfer rates at the surface of the downstream cylinder, particularly within a spanwise region of two and a half diameters from the center of the cross (Fox and Toy, 1988a).

For Case 2 involving an oscillatory cylinder, Shirakashi et al. (1989) and Shirakashi (1994) investigated the effects of adding a stationary cylinder downstream in a cruciform arrangement in a wind tunnel. The Kármán vortex resonance of the upstream cylinder is effectively depressed by the closeness of the downstream cylinder, and vanishes when the gap is smaller than half a cylinder diameter. Then, a new excitation is generated in the same gap range, and this excitation is caused by longitudinal vortices periodically forming near the crossing part of the cylinders.

However, few numerical investigations have been carried out, due to the fact that accurate simulations with the conventional methods based on body-fitted grids in the case of such a complicated configuration are difficult to implement, when moving boundaries are involved. So, it is necessary to utilize a method based on a new concept, such as the virtual boundary method introduced in the current paper.

The aim of this paper is to numerically investigate the flow between two circular cylinders in cruciform arrangement using the virtual boundary method (Goldstein et al., 1993; Fadlun et al., 2000). The numerical method is first validated, and it is demonstrated to be especially suitable for moving boundary problems. Two cases are then considered. For Case 1, two cylinders are stationary at different spacings. For Case 2, the downstream cylinder is considered to be elastic and subjected to transverse vibration in response to the unsteady fluid forces acting on it.

2. Mathematical models

2.1. Governing equations

The nondimensional Navier–Stokes equations for incompressible viscous flow are written as follows:

$$\nabla \cdot \vec{V} = 0,$$

$$\frac{D\vec{V}}{Dt} = -\nabla p + \frac{1}{\mathrm{Re}}\nabla^2 \vec{V} + \vec{F}_{\mathrm{add}}, \tag{1}$$

where $\vec{F}_{\mathrm{add}} = (F_x, F_y, F_z)$ is the added force vector. The diameter D and the uniform free-stream velocity are the characteristic length and velocity, respectively.

The Euler-explicit time discretization scheme is applied to the convective term and the second-order-implicit Crank–Nicholson scheme is used for the viscous term. Spatial derivatives are discretized with the second-order central finite difference. Ignoring the term of $\mathcal{O}(\Delta t^3)$, the finally obtained algebraic equations can be solved using the generic TDMA algorithm in the x, y and z direction sequentially. The pressure is solved from the pressure Poisson equation, which is derived by applying the divergence operator to the momentum equations. The time-dependent term of the pressure Poisson equation is dealt with as by Harlow and Welch (1965), and the derivatives are discretized by a second-order central difference scheme. For detailed description of this method, the reader is referred to Zou et al. (2004, 2005a, b).

2.2. Structural dynamics modeling

The vibrating structure is considered to oscillate in the transverse direction only, and is considered to be a rigid body. It is assumed that the downstream circular cylinder is mounted as a spring-damper-mass system, and the motion of the cylinder can be described by the following equation:

$$\frac{\mathrm{d}^2 z_{\mathrm{obj}}}{\mathrm{d}t^2} + 2\alpha\omega_n \frac{\mathrm{d}z_{\mathrm{obj}}}{\mathrm{d}t} + \omega_n^2 z_{\mathrm{obj}} = \frac{F_l(t)}{m}, \tag{2}$$

where z_{obj} is the instantaneous transverse displacement of the cylinder; α is the damping factor representing the intensity of the damping due to structural dissipation, $\omega_n = \sqrt{k/m} = 2\pi f_n$ is the angular natural frequency of the cylinder, m is the mass per unit length of the cylinder and $F_l(t)$ is the induced lift force. Eq. (2) indicates that the response of the cylinder is a function of the damping factor α, the frequency f_n, the mass ratio M^* ($M^* = m/\rho D^2$) and the lift force $F_l(t)$. It is reasonable to assume that the force term on the right-hand side of the equation is a constant within a time step, as long as the time step is small enough. The equation can be solved easily using the Runge–Kutta method, once the lift force is known from the flow field calculation. The lift force on the cylinder is calculated by integrating the added force field. The response of the cylinder is calculated by solving Eq. (2), and then influences the fluid motion at the next time step.

3. Numerical schemes

3.1. Virtual boundary method

The so-called virtual boundary method was first proposed by Goldstein et al. (1993) to treat the no-slip condition on the boundary immersed in the flow field. The solid domain is assumed filled with fluid, and a virtual body-force term to reflect the effect of the no-slip boundary condition is introduced in the Navier–Stokes equations. The body-force field adopted in their work is governed by a feedback loop. Goldstein et al. (1993) applied this procedure to simulate a start-up flow around a circular cylinder. Fadlun et al. (2000) presented an alternative expression for the added body force. Instead of using a feedback forcing with arbitrary gain, they employed a direct force at as following:

$$\vec{F}^{n+1} = -\overrightarrow{\mathrm{RHS}}^{n} + \frac{\vec{U}^{n+1} - \vec{u}^{n}}{\Delta t}, \tag{3}$$

where $\vec{U}^{n+1}$ is the velocity of solid boundary point at current time level $t + \Delta t$ and $\vec{u}^{n}$ is the corresponding fluid velocity at time level t. The term $\overrightarrow{\mathrm{RHS}}^{n}$ contains the convective, viscous and pressure gradient terms in the momentum equation at time level t. Thus, the boundary condition can be fulfilled at each time level and no rigid stability limit is required after the body force defined by Eq. (3) is introduced into the Navier–Stokes equations. There, the rigid limit in a rigid body is that different parts of a rigid body are prevented from relative movement. In the present study, the added body force given by Eq. (3) is imposed inside the body as well as on the boundary.

Inside the solid body, the added body force can be calculated directly at the grid point using the expression given by Eq. (3). For the grid points near the surface but outside the body, a certain interpolation procedure is needed. Detailed description is given as follows (see Fig. 1). In Fig. 1, $p_f(x_f, y_f, z_f)$ is a grid point near the solid surface and $p_s(x_s, y_s, z_s)$ is the surface point lying on the line connecting p_f and the center of the circle. In order to obtain the added body force $\vec{F}(x_s, y_s, z_s)$ on p_s from Eq. (3), six virtual points are constructed and each point is one grid spacing away from p_s. In Fig. 1, four virtual points, a, b, c and d are displayed and another two virtual points lie in the directions perpendicular

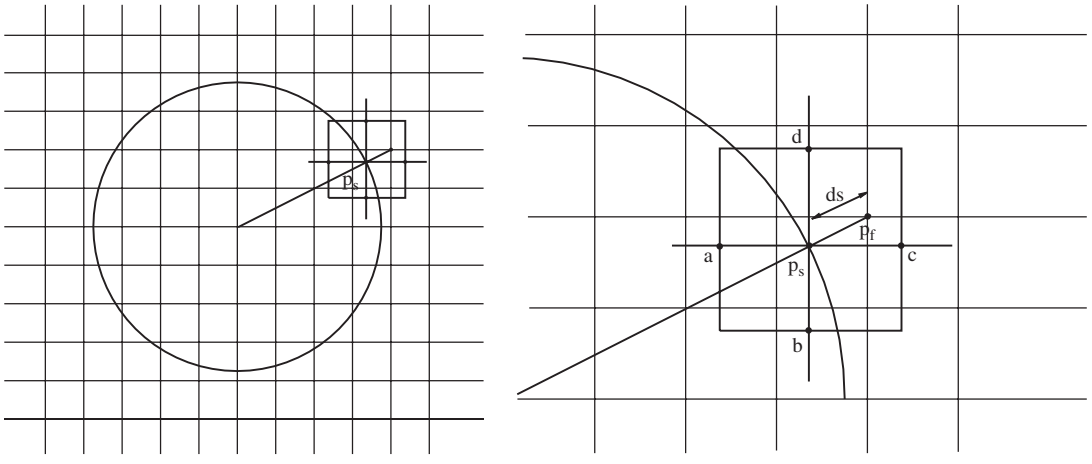

Fig. 1. Body force on the surface is distributed to the grid nearby.

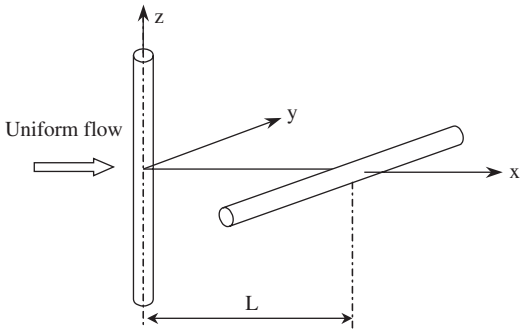

Fig. 2. Model of the computational domain.

to this plane. Using the variables on these six virtual points and the desired boundary velocities on p_s, all first and second derivatives in term $\overrightarrow{\mathrm{RHS}}^n$ can be evaluated at the point p_s. To get the variables on a virtual point, we can use trilinear interpolations with eight computational grid points around it. The effect of the body force $\vec{F}(x_s, y_s, z_s)$ is distributed to the nearby grid point p_f using a linear interpolation, $\vec{F}(x_f, y_f, z_f) = (1 - \mathrm{d}s/\mathrm{d}xyz)\vec{F}(x_s, y_s, z_s)$. Here $\mathrm{d}xyz$ is the diagonal length of the grid element and $\mathrm{d}s$ is the distance between p_s and p_f. It should be noted that the body force is equal to zero for the grid points, if $\mathrm{d}s > \mathrm{d}xyz$ is satisfied.

For a complex geometry, we have developed a search procedure to find a closest point p_s to p_f on the boundary, with the line connecting these two points normal to the boundary. However, for the present case of a relatively simple configuration, we employ the more efficient method introduced earlier.

The main advantage of the current approach is that flows with extremely complex internal boundaries can be simulated with relative ease on simple Cartesian meshes, and the solver for fixed boundary problems is applicable to the moving boundary case conveniently without any modification.

3.2. Computational domain and boundary conditions

In this study, a cuboid flow field is considered with the upstream cylinder located at $8D$ from the inflow boundary, and the distance from the downstream cylinder center to the outflow boundary is $20D$. The dimensions of the computational domain in y and z directions are both $12D$. The origin of the coordinate system is located at the center of the upstream cylinder. The detailed geometric configuration is depicted in Fig. 2. A nonuniform Cartesian grid system is generated in the flow domain. The grid is clustered near the cylinders and the grid spacing is increased in a proper with increasing distance away from the surface of the cylinders.

The boundary conditions employed for the present investigation are as follows: (a) the free-slip conditions are imposed at the transverse confining surfaces: $\partial u/\partial y = v = \partial w/\partial y = 0$, and at the spanwise confining surfaces: $\partial u/\partial z = w = \partial v/\partial z = 0$. Both cylinders extend in their longitudinal directions to the computational boundaries. In the vicinity of the two ends of the cylinders, no interpolation is needed, because we can obtain the velocities from the velocity boundary conditions. (b) At the inlet, a constant streamwise velocity is used, with other velocity components being zero, and the nonreflecting boundary condition is imposed at the outlet: $\partial\vec{u}/\partial t + u_a\partial\vec{u}/\partial n = 0$, where u_a is the averaged streamwise velocity at the outlet, obtained from the velocities at the last time level. By introducing the nonreflecting condition, the computational domain can be greatly reduced in the streamwise direction. (c) The pressure Neumann condition is applied to the inflow, far field and outflow boundaries, and the pressure condition is imposed at half-grid points near the domain boundaries (Abdallah, 1987a, b; Deng et al., 2006).

4. Computational validation

Validation of the numerical method is carried out in three steps; the first is to assess the reliability of the method for a stationary cylinder in two-dimensional flow, the second is to demonstrate the efficiency and accuracy in predicting the dynamic response of an elastic cylinder. The final step is to verify the ability of the method for three-dimensional models, by the simulation of the flow around a three-dimensional cylinder.

4.1. Two-dimensional flow around a circular cylinder

A rectangular domain is employed to simulate the flow over a stationary cylinder. The boundary conditions are imposed in such a way that the flow is from the left toward the right of the domain. A circular cylinder is placed inside the domain with its center being $8D$ away from the inlet and $25D$ away from the outlet. The domain has a transverse dimension of $16D$. These dimensions have been chosen in order to minimize the boundary effects on the flow. Fig. 3 shows the 275×156 nonuniform mesh used in the present studies, and the grid near the cylinder is uniform. The nonreflecting boundary condition is used on the outlet boundary. A uniform constant velocity is imposed at the domain entrance, the top boundary and the bottom boundary.

In order to establish a grid-independent solution, computations have been performed for several meshes at $\mathrm{Re} = 150$. The results obtained with six grid sizes are listed in Table 1 to illustrate the importance of fine near-body grid resolution for the accuracy of the computed results. This grid refinement study is to verify the grid-independence of the results and the accuracy of the method. The mean drag coefficients $C_{d\mathrm{mean}}$ and the nondimensional vortex shedding frequencies (Strouhal numbers St) are presented in Table 1. They become grid independent for a grid size of $\Delta x = \Delta y = 0.05$, therefore all the following simulations are carried out with such a grid size. Our drag coefficients at different Reynolds numbers are compared with other numerical and experimental results, in Table 2. Very good agreement is seen.

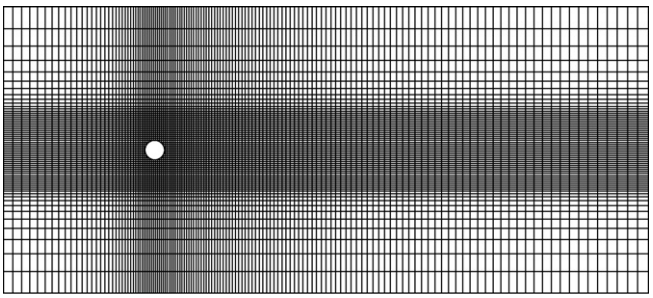

Fig. 3. Nonuniform mesh used for the flow past a two-dimensional circular cylinder. Only every other grid line is shown in both directions.

Table 1
Grid refinement study

$\mathrm{Re} = 150$		
$\Delta x = \Delta y$	$C_{d\mathrm{mean}}$	St
0.100	1.415	0.167
0.075	1.508	0.171
0.065	1.395	0.174
0.055	1.377	0.180
0.050	1.370	0.183
0.045	1.370	0.183

Table 2
Comparison of mean drag coefficient ($C_{d\mathrm{mean}}$) with those of other authors

Reynolds number	10	20	40	47	50	80	100	150
Park et al. (1998)	2.78	2.01	1.51	—	—	1.35	1.33	—
Ye et al. (1999)	—	2.03	1.52	—	—	1.37	—	—
Lima et al. (2003)	2.81	2.04	1.54	1.46	1.46	1.40	1.39	1.37
Present work	2.86	2.03	1.51	1.44	1.43	1.33	1.31	1.37

4.2. Vortex-induced vibrations of an elastic circular cylinder

Flow-induced vibration of an elastic structure is, in general, nonlinear. The vibration of the structure affects the fluid flow around the structure, which in turn modifies the hydrodynamic forces on the structure and hence the structural response. Representative studies carried out on elastic circular cylinders have been reviewed by Williamson and Govardhan (2004). These studies, which covered a range of Reynolds number (Re), showed that the vibration amplitude depends on various parameters. Griffin (1992) derived a reduced damping parameter, $\mathrm{Sg} = 8\pi^2\mathrm{St}^2\alpha M^*$, by analyzing a group of data collected from different experiments. Here, $\mathrm{St} = f_s D/U_\infty$ is the Strouhal number, U_∞ being the uniform inflow velocity and f_s the vortex shedding frequency.

For the case of a stationary circular cylinder at $\mathrm{Re} = 200$, good agreement is obtained in this paper in comparison with previous studies. Our Strouhal number is about 0.195, which agrees well with the experimental result of 0.197 from Williamson (1996a), and the numerical result of 0.196 from Meneghini and Bearman (1995). For the case of an elastic circular cylinder with one degree of transverse freedom the calculations are carried out at $\mathrm{Re} = 200$ and $M^* = 1$. The initial flow field is from the case of the stationary circular cylinder. From its definition, Sg varies with the damping factor α, and in the present study we let Sg vary from 0.01 to 10. In order to catch the maximum value of the vibration amplitude, the frequency ratio is chosen around $f_n/f_s^* = 1.0$, where f_n is the natural frequency of the cylinder and f_s^* the vortex-shedding frequency of the rigid cylinder.

Our peak-to-peak vibration amplitude, $2Y_{\max}/D$ is plotted versus Sg in Fig. 4, together with the numerical results of Newman and Karniadakis (1995), the results of Zhou et al. (1999) and the data collected by Griffin (1992). It can be observed that the present results show a good agreement with the numerical results of Newman and Karniadakis (1995), and Zhou et al. (1999). All simulations show that the amplitude is limited as Sg approaches zero, and they decrease with increasing Sg. The discrepancy between the simulations and the experiments could be due to the difference in the values of the other parameters, such as Re and the mass ratio, and also the three-dimensionality in the wake.

In order to make comparisons with Zhou et al. (1999), the same parameters are chosen for the calculations: $\mathrm{Re} = 200$, $M^* = 1$ and $\mathrm{Sg} = 0.01$. The frequency ratio, f_n/f_s^*, ranges from 0.65 to 5.2. Fig. 5 shows the vortex pattern in two typical cases of the frequency ratio: $f_n/f_s^* = 1.73$ and 1.49 (Fig. 5(a) and 5(b)). At $f_n/f_s^* = 1.49$, the separation distances between vortices in the transverse and streamwise directions and the width of the wake start to change, and two batches of the vortices are seen in Fig. 5(b). Fig. 5(c) and (d) show the results from Zhou et al. (1999) at the same two frequency ratios, and a good qualitative agreement is reached. Fig. 6 shows the time histories of the drag and lift force, together with the cross-flow displacement Y/D of the cylinder. In Fig. 6(a), the lift force and the cross-flow displacement of the cylinder show a beating behavior at $f_n/f_s^* = 1.73$, and a low frequency is observed as a modulating signal. This beating behavior has also been observed by Zhou et al. (1999), as shown in Fig. 6(c). At $f_n/f_s^* = 1.49$, our amplitude of the drag force is a little larger than that obtained by Zhou et al. (1999), as seen from Fig. 6(d). The comparison shows that the present numerical method can predict the response of a elastic cylinder well, both qualitatively and quantitatively.

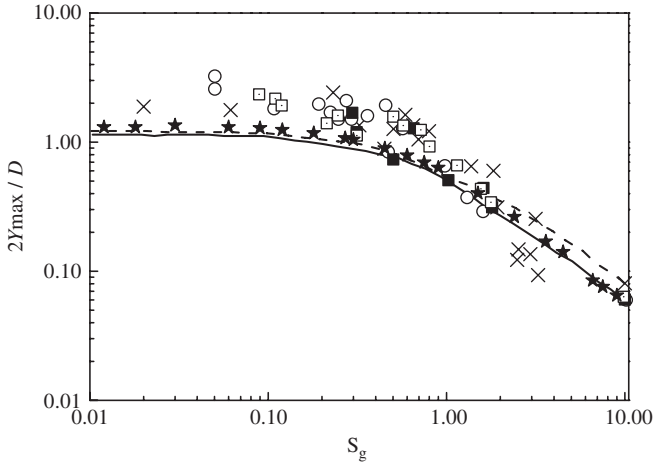

Fig. 4. Flow-induced transverse vibration amplitude versus Sg. Dashed line: calculated results (two-dimensional) of Newman and Karniadakis (1995) for $\mathrm{Re} = 200$ and $M^* = 1$; solid line: calculated results (two-dimensional) of Zhou et al. (1999) for $\mathrm{Re} = 200$ at $M^* = 1$; symbols $\times, \circ, \square, \blacksquare,$: experimental data collected by Griffin (1992); symbol $\star$: present results for $\mathrm{Re} = 200$ and $M^* = 1$.

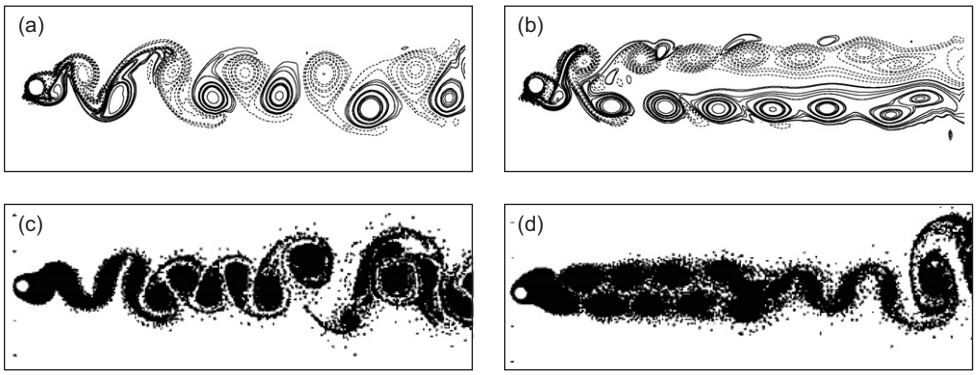

Fig. 5. Vortex pattern in the wake of an elastic cylinder for Sg = 0.01 and $M^* = 1$. (a) $f_n/f_s^* = 1.73$, in present study; (b) $f_n/f_s^* = 1.49$, in present study; (c) $f_n/f_s^* = 1.73$, by Zhou et al. (1999); (d) $f_n/f_s^* = 1.49$, by Zhou et al. (1999).

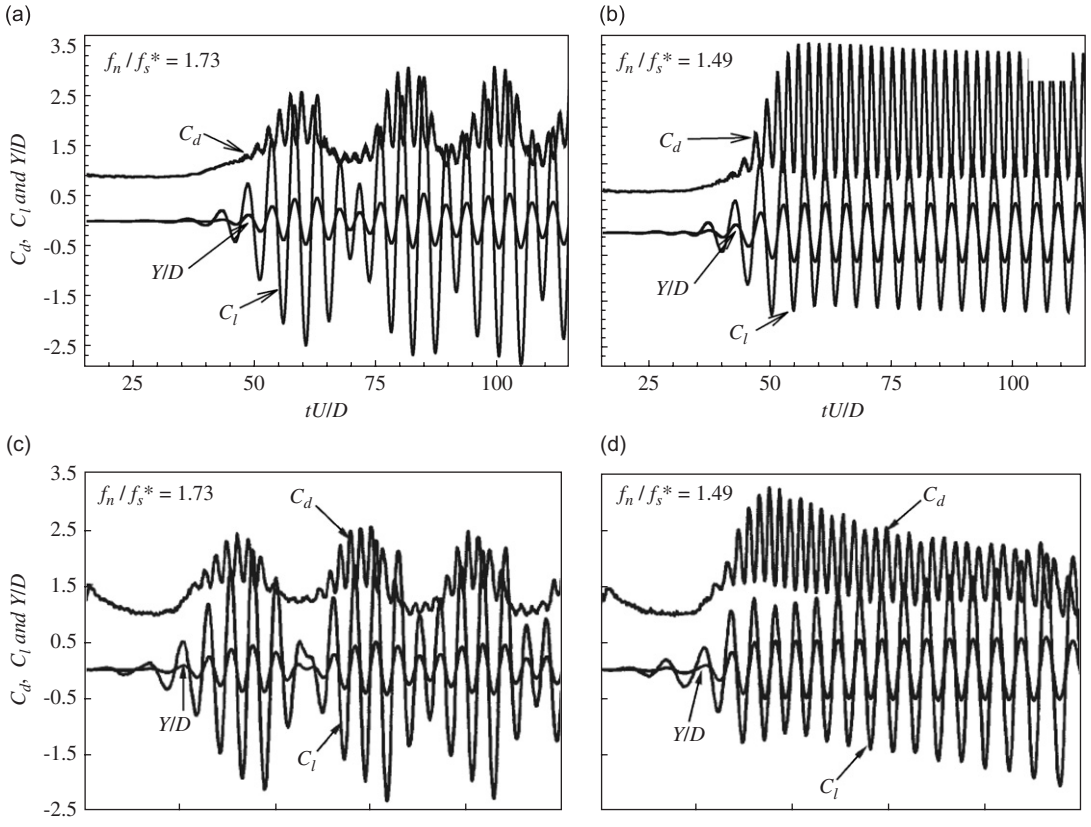

Fig. 6. Time histories of C_d, C_l and Y/D of an elastic cylinder with Sg = 0.01 and $M^* = 1$. (a) $f_n/f_s^* = 1.73$, in present study; (b) $f_n/f_s^* = 1.49$, in present study; (c) $f_n/f_s^* = 1.73$, by Zhou et al. (1999); (d) $f_n/f_s^* = 1.49$, by Zhou et al. (1999).

4.3. Three-dimensional flow around a circular cylinder

In order to prove the ability of the numerical method to deal with three-dimensional problems, the simulation of the flow over a three-dimensional circular cylinder is carried out. The grid in the section of the domain is similar to that used in the case of a two-dimensional cylinder, and the same grid is repeated in all spanwise sections. The wake of a bluff object, in particular a circular cylinder is known to undergo a 'fast' transition from a laminar two-dimensional

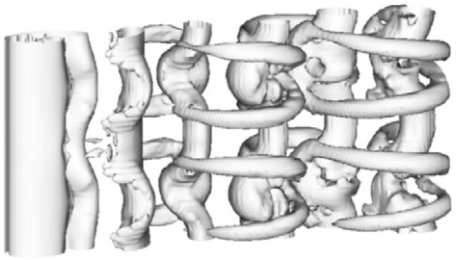

Fig. 7. Three-dimensional vortex structures of a single cylinder obtained by the present study.

state to a turbulent three-dimensional state, and the critical Reynolds number is about 190. The transition regime involves two modes of three-dimensional instability (Mode A and Mode B), depending on the regime of Reynolds number. In this paper, a λ_2-definition (Jeong and Hussain, 1995) is introduced to identify the vortex region. At $Re = 220$, Mode A instability obtained from our present study is presented in Fig. 7, and the corresponding spanwise wavelength is about 4.0 and $St = 0.183$. Williamson (1996a) indicated that the wavelength at $Re = 200$ is 4.01, and suggested a decreasing wavelength as Re increases. Williamson (1996b) found that $St = 0.188$ for $Re = 220$. The wake pattern is also qualitatively comparable to experimental visualizations by Williamson (1992).

5. Results

5.1. Case 1—two stationary cylinders in cruciform arrangement

A simulation of the flow between two stationary circular cylinders in cruciform arrangement is performed first. The side view of the three-dimensional vortex structures is shown in Fig. 8, from which one can observe that the spatial structures of the flow between two stationary cruciform cylinders are different at various spacing ratios. When the spacing ratio $L/D > 3$, the influence of the downstream cylinder on the wake of the upstream cylinder is restricted in the region that the two flow wakes intersect, and out of this region the wake of the upstream cylinder maintains a regular Kármán vortex street. When $L/D \leqslant 3$, the influence of the downstream cylinder to the wake of the upstream one is enlarged, compared to the cases of larger spacing ratio (Fig. 8(c,d)). Two rows of three-dimensional streamwise vortex structures can be observed in both sides of the mixed region.

From Williamson (1996a, b), the physical origin of the three-dimensional small-scale instabilities in the wake of a single circular cylinder has attracted much attention. It has been recognized that the two instabilities scale on two different physical features of the wake flow. The (long-wavelength) Mode A scales on the larger physical feature in the wake flow, namely the primary vortex cores, and is shown to be due to an elliptic instability in these vortices. The (short-wavelength) Mode B, on the other hand, scales on the smaller physical length scale, namely the braid shear layer. In the present case of two circular cylinders in cruciform arrangement at $Re = 150$, the instability of the vortex can be explained by Mode A. When the downstream cylinder is set far enough from the upstream one ($L/D > 3$), the flow shedding from the upstream cylinder looks smooth along the spanwise direction, and only the immediate vortex tubes shedding from the upstream cylinder are extruded towards the upstream direction in the middle part. When $L/D \leqslant 3$, the vortex pair immediately shedding from the upstream cylinder is broken, and there exist no uninjured vortex tubes along the spanwise of the upstream cylinder, as shown in Fig. 8(a, b). From Williamson's theory, the immediate vortex pair in the near wake of the upstream cylinder plays a key character on the instability of the whole wake from the upstream cylinder. When this vortex pair is disturbed, the whole flow wake is changed, then two rows of streamwise vortices come into being in the flow wake as shown in Fig. 8(a, b).

The planform of the three-dimensional vortex structures is shown in Fig. 9. We can observe that the whole wake along the spanwise of the downstream cylinder is disordered, irrespective of the spacing between these two cylinders. It can be concluded that the vortex shedding from the upstream cylinder will exert an impact on the downstream cylinder and disturb all vortex tubes shedding from the downstream cylinder, including the immediate vortex pair behind it. There is no stable region in the whole wake as shown in Fig. 9.

The lift coefficient time histories for different spacings are shown in Fig. 10. It is interesting to note that for $L/D = 4$ and $L/D = 8$, the lift amplitude of the downstream cylinder is smaller than that of the upstream cylinder. This is in sharp contrast to the case for two cylinders in a tandem arrangement, where the lift amplitude for the downstream

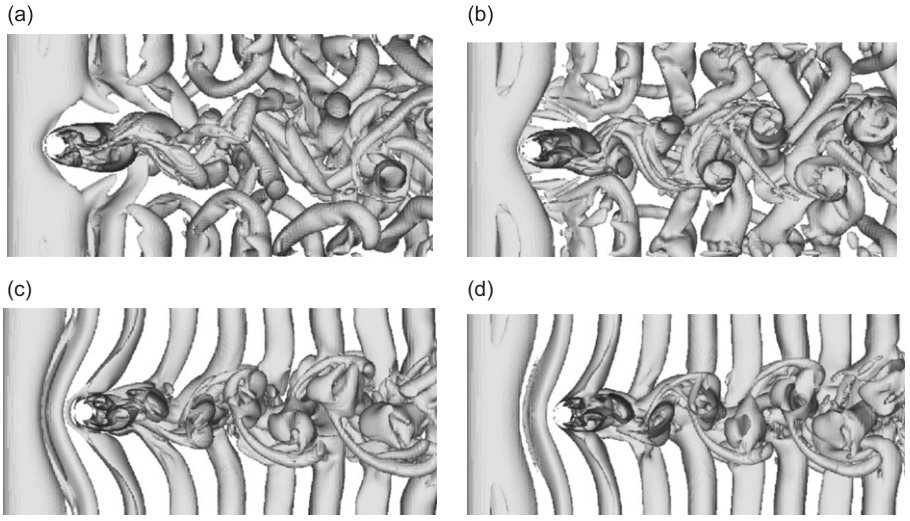

Fig. 8. Side-view of the three-dimensional vortex structures (from negative to positive direction in the y-axis): (a) $L/D = 2$; (b) $L/D = 3$; (c) $L/D = 4$; (d) $L/D = 5$.

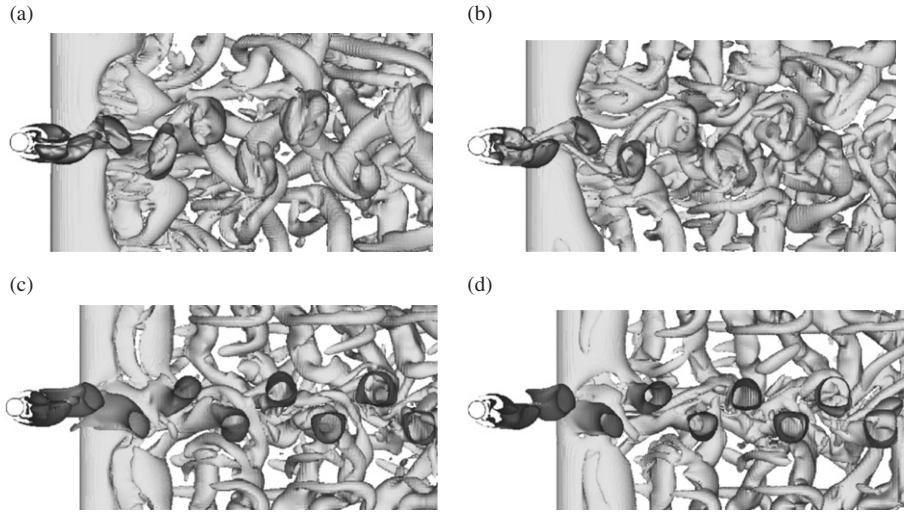

Fig. 9. Planform of the three-dimensional vortex structures (from positive to negative direction in the z-axis): (a) $L/D = 2$; (b) $L/D = 3$; (c) $L/D = 4$; (d) $L/D = 5$.

cylinder is in general greater than that of the upstream one, due to the disturbed flow shedding from the upstream cylinder. From Fig. 10, one can also find that for the upstream cylinder, when the spacing ratio is increased from 3 to 4, a very significant change occurs. The peak-to-peak value of the lift coefficient for the upstream cylinder at $L/D = 4$ is almost three times as great as that for $L/D = 3$.

Fourier analysis of the velocities is performed, and the spatial point of interest is put in the near wake of the downstream cylinder. The spectral energy distributions for various cases of spacing are presented in Fig. 11. The corresponding Strouhal number increases with the increasing of the spacing ratio, as shown in Fig. 11. When $L/D = 2$, the peak energy measured at the dominant frequency is about half of that found in other cases.

Measurements of the mean pressure distribution on the rear stagnant points of the upstream cylinder are taken for the spacings varying from $L/D = 2$ to 8, as shown in Fig. 12. Values of the coefficient of pressure, C_p, were calculated

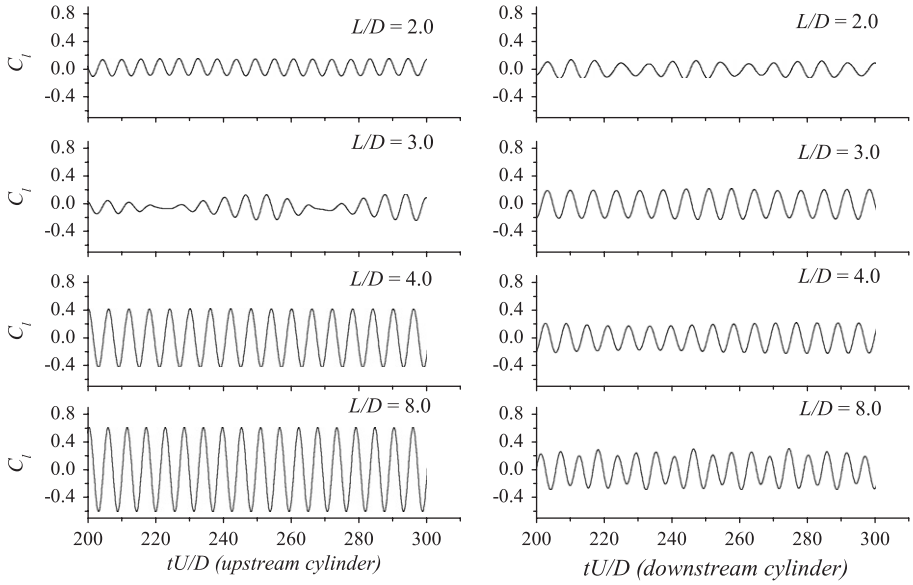

Fig. 10. Lift coefficient time histories for different spacings. Left: the upstream cylinder; right: the downstream cylinder.

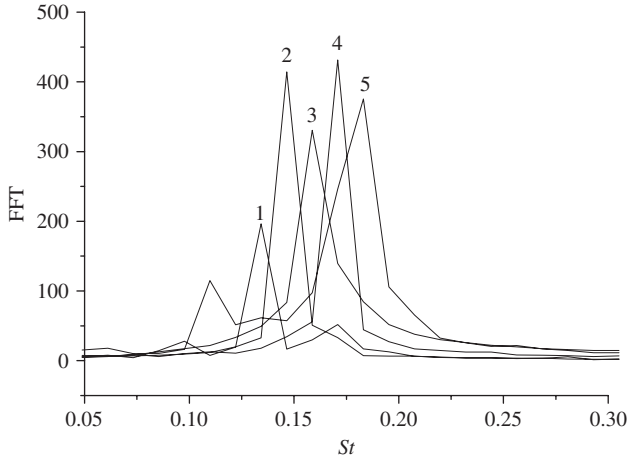

Fig. 11. Spectral energy distributions recorded in the wake of the downstream cylinder for different spacings: 1, $L/D = 2$; 2, $L/D = 3$; 3, $L/D = 4$; 4, $L/D = 5$; 5, $L/D = 8$.

with the expression

$$C_p = \frac{P_L - P_0}{\frac{1}{2}\rho U_0^2},$$

where P_L is the local surface pressure, P_0 is the free-stream static pressure, and $\frac{1}{2}\rho U_0^2$ is the dynamic head of the free-stream. In the present study, the reference point is located at the center of the inflow surface. When the two cylinders are close enough, as for $L/D = 2$, the profile displays a unique curve with a peak found around the center of the configuration. As shown in Fig. 12, a peak value of -0.3 is reached around the position $z/D = 0$ for $L/D = 2$, and the value of C_p for other cases are all around $C_p = -1$. From Fig. 12, we can notice that the two curves for $L/D = 2$ and $L/D = 3$ are not similar. This is due to the different attributes in the gap between the two cylinders for $L/D = 2$ and 3. Fox and Toy (1988a) observed that when the distance between the cylinders is less than three diameters, i.e., $L/D < 3$, two stationary recirculation cells are present in the gap formed at the center of the cross, whereas at spacings beyond

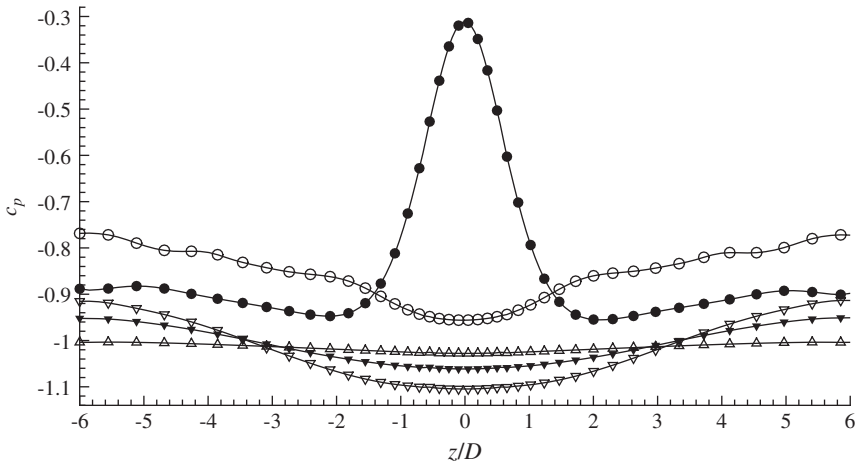

Fig. 12. Mean base-pressure distributions on the upstream cylinder; •, $L/D = 2$; ○, $L/D = 3$; ▽, $L/D = 4$; ▼, $L/D = 5$; △, $L/D = 8$.

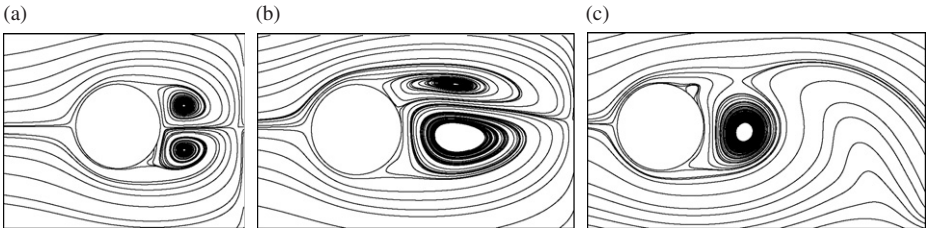

Fig. 13. The planar streamlines in the near wake of the upstream cylinder, in the x–y plane at the center of the gap for $z = 0$. (a) $L/D = 2$; (b) $L/D = 3$; (c) $L/D = 4$.

three diameters, i.e. $L/D > 3$, these cells are replaced by vortex shedding in the wake of the central portion of the upstream cylinder. In this paper, it is suggested that the $L/D \leqslant 3$ region can be further subdivided into subregions, similar to that of two tandem cylinders (Slaouti and Stansby, 1992). For $L/D = 3$, a distance larger than the length of the recirculation region of a single cylinder, intermittent vortex shedding is observed behind the upstream cylinder, and this can be regarded as a transitional state from the state of two steady recirculation cells formed in the gap to the state of the periodic vortex shedding from the upstream cylinder. Fig. 13 shows the streamlines in the x–y plane at $z = 0$. From Fig. 13(a)–(c), three types of flow pattern clearly exist. The recirculation cells for $L/D = 2$, however, do not persist in the spanwise direction of the upstream cylinder, since the constraint from the downstream one is not present beyond the center of the configuration.

In order to examine the influence of the vortex shedding from the upstream cylinder on the hydrodynamic force on the downstream cylinder, the spanwise distributions of the stagnant pressure on the downstream cylinder are presented in Fig. 14. The results show that, regardless of the member spacing, the modification of the pressure on the downstream cylinder due to the presence of the upstream cylinder is largely confined to a region of five diameters, $-2.5D \leqslant z \leqslant 2.5D$. The stagnant pressures in the undisturbed outer region have values equal to those found at corresponding locations on a single cylinder, whereas those within the inner region are decreased to a minimum at the center of the span, in excellent agreement with the results obtained by Fox and Toy (1988a). For $L/D = 2$ and 3 in Fig. 14, two troughs are observed, indicating the reattachment of the separated shear layer from the upstream cylinder to the downstream cylinder.

5.2. *Case 2—a stationary cylinder and a downstream elastic cylinder in cruciform arrangement*

In this case, the spacing is chosen to be $L/D = 4$ and 5. The mass ratio $M^* = 10$ and the damping factor $\alpha = 0.0038$. The simulations of the flow around an isolated elastic cylinder with the same group of parameters are also carried out

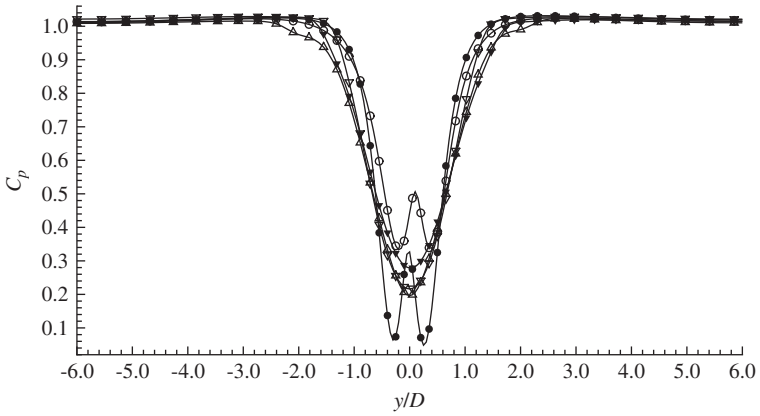

Fig. 14. Mean stagnation pressure distributions on the downstream cylinder; •, $L/D = 2$; ○, $L/D = 3$; ▽, $L/D = 4$; ▼, $L/D = 5$; △, $L/D = 8$.

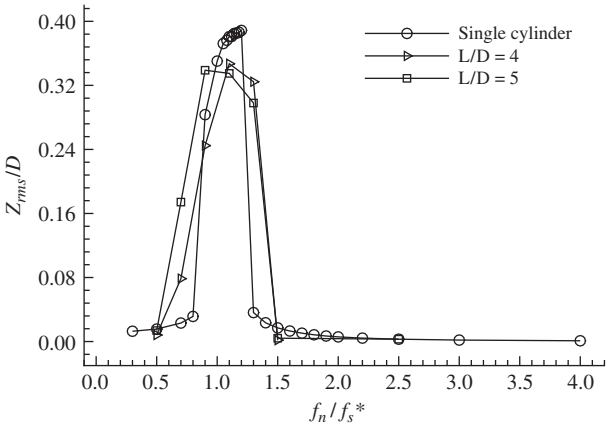

Fig. 15. Variation of Z_{rms}/D with f_n/f_s^*.

for comparison. From Williamson and Govardhan (2004), there is an important question debated for about 25 years. The question is whether a combined mass-damping parameter could reasonably collapse peak-amplitude data in the Griffin plot. Different mass-damping parameters have been used in several studies, including the combined response parameter Sg, so termed by Skop (1974). Despite the enormous effort over the last 25 years, the question is not yet fully resolved. In this paper, we select fixed parameters of mass ratio and damping factor in all cases, just in order to make a comparison.

In order to obtain a significant vortex-induced response, the frequency ratio f_n/f_s^* is chosen from 0.5 to 1.5, here f_s^* denoting the vortex-shedding frequency of the rigid cylinder and f_n denoting the natural frequency of the structure. The root-mean-square values of the cross-flow amplitude Z_{rms} and the mean drag coefficient $C_{d\mathrm{mean}}$ of the downstream cylinder versus the frequency ratio are shown in Figs. 15 and 16, respectively. The vortex-induced responses of a single circular cylinder are also plotted. We can observe that the peak value of the vibrations for a single cylinder occurs at $f_n/f_s^* = 1.20$. From Zhou et al. (1999), this offset from $f_n/f_s^* = 1.0$ is related to the added mass on the natural frequency of the fluid–structure system. In Fig. 15, the results further show that the peak amplitude Z_{rms}/D for $L/D = 4$ and 5 is lower than that of a single cylinder, and the peak bands of Z_{rms}/D are wider for the cruciform arrangement cases, indicating that a cylinder immersed in the wake of an upstream one in a cruciform arrangement has a wider resonance region.

Figs. 17 and 18 show the time histories of the force coefficients and the displacement, with the frequency ratio descending from $f_n/f_s^* = 1.1$ to 0.5 in Fig. 17, and the frequency ratio ascending from $f_n/f_s^* = 1.1$ to 1.5 in Fig. 18. The computation for the case of $f_n/f_s^* = 1.1$ starts from an initial flow field where the continuity condition is satisfied. The displacement varies with the frequency ratio, and reaches zero for the frequency ratio small or great enough.

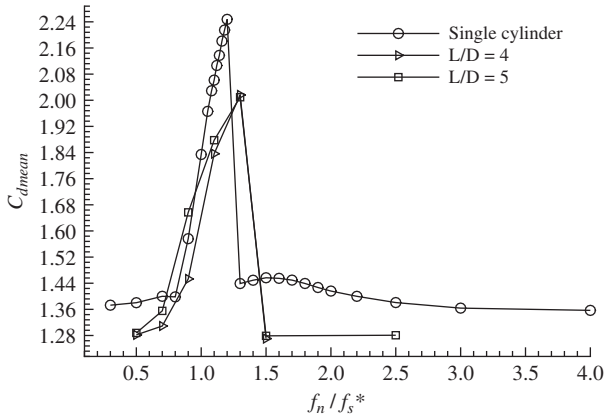

Fig. 16. Variation of the mean drag coefficient with f_n/f_s^*.

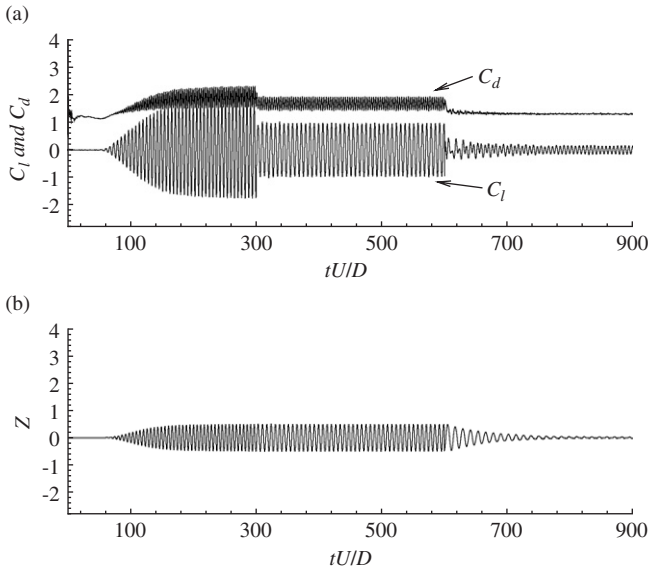

Fig. 17. Force coefficients and displacement time histories at different frequency ratios: $f_n/f_s^* = 1.1$, $tU/D = 0-300$; $f_n/f_s^* = 0.9$, $tU/D = 300-600$; $f_n/f_s^* = 0.5$, $tU/D = 600-900$.

It is well known that for the case of a single cylinder, the vortex pattern is very similar to the one for the stationary cylinder when the natural frequency of the cylinder is far away from the vortex shedding frequency. As the frequency ratio decreases or increases to the resonance value, the cylinder vibration starts to affect the vortex pattern in the wake. Fig. 19 shows the comparison of the planar vortex pattern in the wake of the downstream cylinder at frequency ratio $f_n/f_s^* = 0.5$ and 1.1 for $L/D = 5$. Two planes are intercepted at $y = 4$ and 0 for both cases. From Fig. 19(a) and (c), one can observe that in the plane far away from the central region of the cross, the vortices shed from the downstream cylinder form two parallel rows of the vortices in the near wake. The vortex spacing appears to become smaller in the streamwise direction and wider in the transverse direction when the frequency ratio approaches the resonance value, as shown in Fig. 19(c) for $f_n/f_s^* = 1.1$. Such a spacing change is due to the fact that the vortices are shed at a higher frequency in this case, thus leading to a narrowing of the streamwise distance between the vortices. In the x–z plane at $y = 4$, the wake has not been affected by the upstream cylinder, so is similar to that from an isolated cylinder. In the plane at the center of the cruciform structure (of, i.e., $y = 0$), although the wake of the downstream

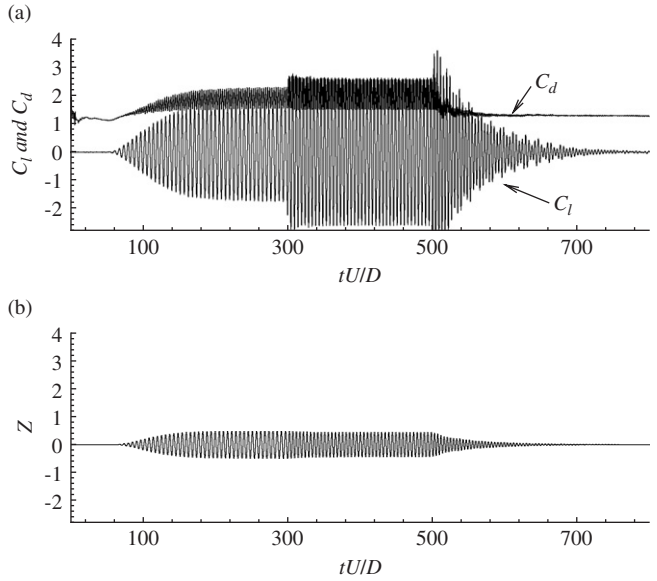

Fig. 18. Force coefficients and displacement time histories at different frequency ratios: $f_n/f_s^* = 1.1$, $tU/D = 0-300$; $f_n/f_s^* = 1.3$, $tU/D = 300-500$; $f_n/f_s^* = 1.5$, $tU/D = 500-800$.

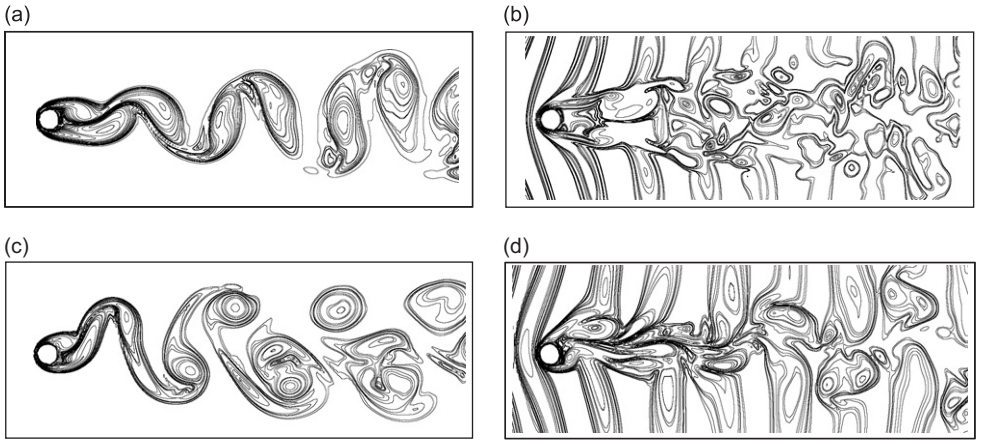

Fig. 19. Vortex pattern in x–z plane for $L/D = 5$: (a) $f_n/f_s^* = 0.5$, $y = 4$; (b) $f_n/f_s^* = 0.5$, $y = 0$; (c) $f_n/f_s^* = 1.1$, $y = 4$; (d) $f_n/f_s^* = 1.1$, $y = 0$.

cylinder for both cases is affected by the vortices shedding from the upstream cylinder, the flow pattern in the case of $f_n/f_s^* = 1.1$ appears more organized, and there exist more small eddies in the case of $f_n/f_s^* = 0.5$, as shown in Fig. 19(b) and (d).

In Fig. 20, three-dimensional vortex structures are shown for $L/D = 5$ at $f_n/f_s^* = 0.5$ and 1.1 using the λ_2-definition. One can observe that the streamwise vortex structures for $f_n/f_s^* = 1.1$ are smaller and quantitatively fewer than those for $f_n/f_s^* = 0.5$. This can be observed more clearly in Fig. 21, which shows the iso-surfaces of the streamwise vortices for $L/D = 4$, and the black denotes $\omega_x = 0.3$, the gray denotes $\omega_x = -0.3$. Two rows of vortices are clearly seen near the lateral surfaces of the computational domain in Fig. 21(a), and when the frequency ratio is increased to $f_n/f_s^* = 1.1$, which falls in the resonance region, these two rows of vortices move to the mixed region, as shown in Fig. 21(b).

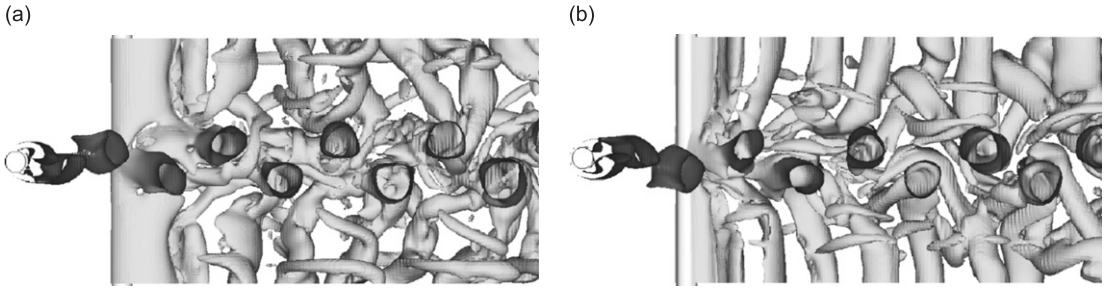

Fig. 20. Three-dimensional vortex structures for $L/D = 5$ (top view): (a) $f_n/f_s^* = 0.5$; (b) $f_n/f_s^* = 1.1$.

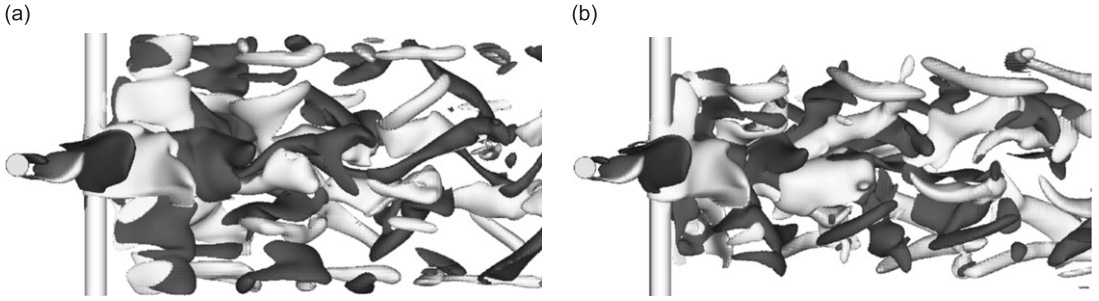

Fig. 21. Iso-surfaces of streamwise vortices for $L/D = 4$ (top view): (a) $f_n/f_s^* = 0.5$; (b) $f_n/f_s^* = 1.1$.

Another phenomenon should be noted. For $f_n/f_s^* = 0.5$, the wake forms a '>' pattern, whereas for $f_n/f_s^* = 1.1$, the wake forms a '<' pattern, as shown in Fig. 20. This phenomenon is also called vortex dislocation, and is generated between the spanwise cells due to the out-of-phase movement of the primary vortex in each cell. Following Williamson (1996a, b), two types of vortex dislocations can be identified. In one, a rather twisted web of vortex linking occurs across the cell boundaries. Such a dislocation is one sided and lacks symmetry. The vortex dislocation in the present study belongs to the second category, where the two-sided dislocation occurs due to the local phase variation in the middle plane of the flow wake. The vortex shedding from the upstream cylinder disturbs the wake of the downstream cylinder, and makes the wake at the central region less sensitive to the vibrations. That is to say, due to the vibrations of the downstream cylinder at different frequency ratios, the central flow wake cannot keep pace with the wake far away from the center.

6. Conclusions

The results from an extensive numerical investigation have provided details of the wake characteristics associated with two circular cylinders arranged perpendicular to each other in a uniform flow. When the downstream cylinder is stationary, the spacing between two cylinders ranges from $L/D = 2$ to 8 and the Reynolds number is kept at $\mathrm{Re} = 150$. Two fundamental flow patterns are found, which is related to a critical cylinder spacing. For $L/D \leqslant 3$, two recirculation cells are present in the gap formed at the center of the cross, whereas for $L/D > 3$, these cells are replaced by periodic vortex shedding from the upstream cylinder. Another effect of the spacing variation on the flow is that for $L/D > 3$, the modification of the wake of the upstream cylinder due to the presence of the downstream cylinder is limited to the mixed region, whereas for $L/D \leqslant 3$ the influenced region is significantly enlarged.

When the downstream cylinder is elastic, two representative cases of spacing, $L/D = 4$ and $L/D = 5$, are investigated. The spacings are greater than the critical value obtained above. We compared the results with that from the vortex-induced vibration of an isolated circular cylinder, and the comparisons are listed below:

(i) The peak amplitude Z_{rms}/D for $L/D = 4$ and 5 is lower than that for a single cylinder, and the resonance region is wider for the cruciform arrangement cases than that of a single cylinder.

(ii) In the x–z plane far away from the center of the cross, the vortex shedding behaves like that of a single vibrating cylinder. In the plane at the center of the configuration, although both cases suffer from the vortices shedding from the upstream cylinder, the case in the resonant region looks more organized.
(iii) When $f_n/f_s^* = 0.5$, the whole flow wake looks like a '>' pattern, and when $f_n/f_s^* = 1.1$ the flow wake forms a '<' pattern. This is due to the local phase variation in the middle plane of the flow wake.

Acknowledgments

The authors wish to thank the financial support of the National Natural Science Foundation of PR China (Grant No. 10272094, 10472104) and the National Basic Research Program of China (No. 2006 CB705400). All these numerical computations have been performed at the Center for Engineering and Scientific Computation (CESC), Zhejiang University. The authors are grateful for this assistance.

References

Abdallah, S., 1987a. Numerical solutions for the pressure poisson equation with Neumann boundary conditions using a non-staggered grid, I. Journal of Computational Physics 79, 182–192.
Abdallah, S., 1987b. Numerical solutions for incompressible Navier–Stokes equations in primitive variables using a non-staggered grid, II. Journal of Computational Physics 79, 193–202.
Bearman, P.W., 1984. Vortex shedding from oscillating bluff body. Annual Review of Fluid Mechanics 16, 195–222.
Blevins, R.D., 1990. Flow-Induced Vibration. Van Nostrand Reinhold, New York.
Brika, D., Laneville, A., 1999. The flow interaction between a stationary cylinder and a downstream flexible cylinder. Journal of Fluids and Structures 13, 579–606.
Deng, J., Ren, A.L., Zou, J.F., Shao, X.M., 2006. Three-dimensional flow around two circular cylinders in tandem arrangement. Fluid Dynamics Research 38, 386–404.
Fadlun, E.A., Verzicco, R., Orlandi, P., et al., 2000. Combined immersed-boundary finite-difference methods for three-dimensional complex flow simulations. Journal of Computational Physics 161, 35–60.
Fox, T.A., 1991. Wake characteristics of two circular cylinders arranged perpendicular the each other. ASME Journal of Fluids Engineering 113, 45–50.
Fox, T.A., Toy, N., 1988a. Fluid flow at the center of a cross composed of tubes. International Journal of Heat and Fluid Flow 9, 53–61.
Fox, T.A., Toy, N., 1988b. The generation of turbulence from displaced crossmembers in uniform flow. Experiments in Fluids 6, 172–178.
Goldstein, D., Handler, R., Sirovich, L., 1993. Modeling a no-slip flow boundary with an external force field. Journal of Computational Physics 105, 354–366.
Griffin, O.M., 1971. The unsteady wake of an oscillating cylinder at low Reynolds number. Journal of Applied Mechanics 38, 729–738.
Griffin, O.M., 1992. Vortex-induced vibrations of marine structures in uniform and sheared currents. NSF Workshop on Riser Dynamics, University of Michigan, USA.
Harlow, F.H., Welch, J.E., 1965. Numerical calculation of time-dependent viscous incompressible flow of fluid with free surface. Physics of Fluids 8, 2182–2189.
Jeong, J., Hussain, F., 1995. On the identification of a vortex. Journal of Fluid Mechanics 285, 69–94.
Lima, A.L.F., Silva, E., Silveira-Neto, A., Damasceno, J.J.R., 2003. Numerical simulation of two-dimensional flows over a circular cylinder using the immersed boundary method. Journal of Computation Physics 189, 351–370.
Liu, Y., So, R.M.C., Lau, Y.L., Zhou, Y., 2001. Numerical studies of two side-by-side elastic cylinders in a cross-flow. Journal of Fluids and Structures 15, 1009–1030.
Meneghini, J.R., Bearman, P.W., 1995. Numerical simulation of high amplitude oscillatory flow about a circular cylinder. Journal of Fluids and Structures 9, 435–455.
Mittal, S., Kumar, V., 1999. Finite element study of vortex-induced cross-flow and in-line oscillations of a circular cylinder at low Reynolds number. International Journal for Numerical Methods in Fluids 31, 1087–1120.
Mittal, S., Kumar, V., 2001. Flow-induced oscillations of two cylinders in tandem and staggered arrangements. Journal of Fluids and Structures 15, 717–736.
Mittal, S., Tezduyar, T.E., 1992. A finite element study of incompressible flows past oscillating cylinders and airfoils. International Journal for Numerical Methods in Fluids 15, 1073–1118.
Mittal, S., Ratner, A., Hastreiter, D., Tezduyar, T.E., 1991. Space–time finite element computation of incompressible flows with emphasis on flows involving oscillating cylinders. International Video Journal of Engineering Research 1, 83–96.
Newman, D.J., Karniadakis, G.E., 1995. Direct numerical simulations of flow over a flexible cable. In: Bearman, P.W. (Ed.), Flow-Induced Vibration. Balkema, Rotterdam, pp. 193–203.

Ohya, Y., Okajima, A., Hayashi, M., 1989. Wake interference and vortex shedding. In: Cheremisinoff, N. (Ed.), Encyclopedia of Fluid Mechanics, vol. 8. Gulf Publishing Co., Houston, pp. 322–389 (Chapter 10).

Ongoren, A., Rockwell, D., 1988a. Flow structure from an oscillating cylinder. Part 1: mechanisms of phase shift and recovery in the near wake. Journal of Fluid Mechanics 191, 197–223.

Ongoren, A., Rockwell, D., 1988b. Flow structure from an oscillating cylinder. Part 2: mode competition in the near wake. Journal of Fluid Mechanics 191, 225–245.

Park, J., Kwon, K., Choi, H., 1998. Numerical solutions of flow past a circular cylinder at Reynolds number up to 160. KSME International Journal 12, 1200.

Shirakashi, M., 1994. Characteristics of periodic vortex shedding from two cylinders in cruciform arrangement. Journal of Fluids and Structures 8, 239–256.

Shirakashi, M., Mizuguchi, K., Bae, H.M., 1989. Flow-induced excitation of an elastically-supported cylinder caused by another located downstream in cruciform arrangement. Journal of Fluids and Structures 3, 595–607.

Skop, R.A., 1974. On modeling vortex-excited oscillations. NRL Memo, Report, 2927.

Slaouti, A., Stansby, P.K., 1992. Flow around two circular cylinders by the random-vortex method. Journal of Fluids and Structures 6, 641–670.

Williamson, C.H.K., 1992. The natural and forced formation of spot-like vortex dislocations in the transition of a wake. Journal of Fluid Mechanics 243, 393–441.

Williamson, C.H.K., 1996a. Vortex dynamics in the cylinder wake. Annual Review of Fluid Mechanics 28, 477–518.

Williamson, C.H.K., 1996b. Three-dimensional wake transition. Journal of Fluid Mechanics 328, 345–407.

Williamson, C.H.K., Govardhan, R., 2004. Vortex-induced vibrations. Annual Review of Fluid Mechanics 36, 413–455.

Williamson, C.H.K., Roshko, A., 1988. Vortex formation in the wake of an oscillating cylinder. Journal of Fluids and Structures 2, 355–381.

Ye, T., Mittal, R., Udaykumar, H.S., Shyyy, W., 1999. An accurate Cartesian grid method for viscous incompressible flows with complex boundaries. Journal of Computational Physics 156, 209–240.

Zdravkovich, M.M., 1977. Review of flow interference between two circular cylinders in various arrangements. ASME Journal of Fluids Engineering 99, 618–633.

Zdravkovich, M.M., 1985. Flow induced oscillations of two interfering circular cylinders. Journal of Sound and Vibration 101, 511–521.

Zhou, C.Y., So, R.M.C., Lam, K., 1999. Vortex-induced vibrations of an elastic circular cylinder. Journal of Fluids and Structures 13, 165–189.

Zou, J., Ren, A., Deng, J., 2004. Study on forced system of two cylinders with various spacing. China Ocean Engineering 18, 391–402.

Zou, J., Ren, A., Deng, J., 2005a. wake structures of two spheres in tandem arrangement at various gaps for $Re = 300$. Progress in Natural Science 15, 19–23.

Zou, J., Ren, A., Deng, J., Shao, X., 2005b. Study on flow past two spheres in tandem arrangement using a local mesh refinement Virtual Boundary Method. International Journal for Numerical Methods in Fluids 49, 465–488.